Development of an MRI/FEA Framework for Analysis of Subject-Specific Aortic Compliance: Part II- Constitutive Law Development and Prediction of Heterogeneous vessel Composition and Deformation

Concannon J[1], Hynes N[2], Sultan S[2], McHugh PE[1], Moerman K[1,3], McGarry JP[1]

[1] Biomedical Engineering, National University of Ireland Galway.

[2] Department of Vascular and Endovascular Surgery, National University of Ireland Galway.

[3] Biomechatronics, Media Lab, Massachusetts Institute of Technology, Cambridge, MA, USA.

Corresponding Author: Patrick McGarry

Email: patrick.mcgarry@nuigalway.ie

Tel: +353 (0)91 493165

Abstract

This paper, the second of two parts, presents a novel subject-specific *in-silico* framework in which we uncover the relationship between the spatially varying constituents of the aorta and the non-linear compliance of the vessel during the cardiac cycle uncovered in Part I. In Part II a novel microstructurally motivated constitutive model is developed, and simulations reveal that internal vessel contractility, due to pre-stretched elastin and actively generated smooth muscle stress, must be incorporated, along with collagen strain stiffening, in order to accurately predict the non-linear pressure-area relationship observed *in-vivo*. Modelling of elastin and smooth muscle contractility allows for the identification of the reference vessel configuration at zero-lumen pressure, in addition to accurately predicting high- and low-compliance regimes under a physiological range of pressures. This modelling approach is also shown to capture the key features of elastin and SMC knockout experiments. The volume fractions of the constituent components of the aortic material model were computed so that the *in-silico* pressure-area curves accurately predict the corresponding MRI data at each location. Simulations reveal that collagen and smooth muscle volume fractions increase distally, while elastin volume fraction decreases distally, consistent with reported histological data. Furthermore, the strain at which collagen transitions from low to high stiffness is lower in the abdominal aorta, again supporting the histological finding that collagen waviness is lower in this distally. The analyses presented in this paper provides new insights into the heterogeneous structure-function relationship that underlies aortic biomechanics. This novel

subject-specific MRI/FEA methodology provides a foundation for personalised *in-silico* clinical analysis and tailored aortic device development.

Keywords: in-vivo mechanical characterization, physical based constitutive law, elastin pre-stretch, collagen stiffening, SMC contractility.

1 Introduction

Regional heterogeneity in the biomechanics of the aorta is a key feature that ensures optimal function of the cardiovascular system. In general, a high level of elastic compliance is required in the proximal aorta, so that the kinetic energy expelled during systole can be stored as elastic strain energy in the vessel, leading to subsequent augmentation of pressure pulse propagation during diastole due to elastic recoil of the wall. The distal aorta, however, takes an alternative approach to blood transfer with a higher smooth muscle cell (SMC) content and a reduced requirement for elastin.

A significant body of literature exists on the experimental testing of aortic tissue, in particular material characterization through uniaxial and biaxial tensile tests [1]–[9]. Due to both the ethical and logistical constraints surrounding the destructive testing of human tissue, animal data exceeds that of humans in the literature. The majority of material characterization of the human aorta is performed on surgically excised samples, for example during the open surgical repair of an abdominal or thoracic aortic aneurysm [1], [10]–[13]. The tissue obtained is in this case however, is (i) too localised to capture the spatially varying biomechanics of the aorta, and (ii) diseased. An alternative approach exists in the testing of aortic tissue post-autopsy; however, further ethical and logistical difficulties exist here, and as such, few studies with this design exist in the literature [14]–[16]. The limitation of this approach is that the tissue is dead, raising concerns about the applicability of such results which ultimately cannot be compared to unknown ‘live’ tissue properties.

In characterizing the mechanical properties of the aorta experimentally, particular focus has been directed towards the effects of ageing. Hallock and Benson [17] found that young aortic tissue exhibits a high degree of extensibility through a bi-concave s-shaped pressure-volume relationship, while in older tissue the total increase in volume is lower and at high pressures the slope of the pressure-volume relationship tends towards a straight horizontal line. Additionally, Vande Geest, & Vorp, [15] found that an older cohort exhibited a much stiffer exponential shaped stress-strain response compared to the younger cohort, with such a notable difference that different forms of strain energy functions were used for

younger and older cohorts (polynomial and exponential forms, respectively). Investigation of aortic heterogeneity has typically relied on *ex-vivo* testing of excised porcine/canine tissue [18], [19]. A biomechanical study of excised canine aortae by Tanaka and Fung [20], reports that proximal samples exhibit a higher compliance than distal samples. A study on the equibiaxial tension behaviour of human aortic samples following autopsy by Haskett [21] reported that the overall compliance decreases with distance from the heart in a cohort less than 30 years of age.

Investigation of the volume fractions of individual wall constituents can provide insight into the local behaviour of the arterial tissue [9], [22]. Harkness [23] reported that the volume fraction of elastin is approximately twice as high as that of collagen in intrathoracic canine aorta. In all other arteries the volume fraction of collagen was found to exceed that of elastin. Saey [24] reported a greater concentration of collagen in the distal thoracic equine aorta than in proximal sections. Davidson [25] reported lower concentrations of elastin fibres in the abdominal regions of porcine aorta than in thoracic regions. Recently, Concannon [26] found that elastin volume fraction decreases, and collagen increases with distance from the heart in the human aorta.

Despite extensive *in-vitro* mechanical testing and histological analysis of excised tissue, few studies to date have attempted to characterise the *in-vivo* biomechanical behaviour of the aorta using non-invasive methodologies. Previous *in-vivo* MRI analyses of the human aorta have focused on limited isolated segments, such as the thoracic [27] or abdominal aorta [28]. Such a focus on a single region does not provide insight into the significant spatial variation in aortic biomechanical behaviour. This limitation is addressed in Part I, whereby a dual-VENC 4D Flow MRI sequence is developed and implemented in a commercial scanner, providing high resolution measurements of aortic deformation at all locations throughout the entire cardiac cycle.

This study develops a subject-specific MRI/FEA framework to uncover the biomechanisms underlying the spatially varying non-linear aortic compliance measured *in-vivo* in Part I. A constitutive law is developed to incorporate the biomechanical contributions of pre-stretched elastin, contractile SMCs, and strain stiffening collagen. Firstly, the role of pre-stretched elastin is investigated. In particular, analyses are performed to identify an equilibrium vessel configuration at zero applied lumen pressure, which is observed to be critical step required in order to predict the key features of the pressure-area relationship observed *in-vivo*. The role of elastin pre-stretch on the lumen pressure at which the aorta transitions from a high compliance to a low compliance regime due to collagen strain

stiffening, is also investigated. A subject-specific FE model is generated directly from the MRI data presented in Part I and the *in-vivo* pressure-area curves are fit using the constitutive law. Finally, the volume fractions of the constituent components of the aortic wall (elastin, collagen and SMCs) are computed throughout the subject-specific aortic FE model and excellent agreement is found with the histological analyses presented in [26].

2 Methodology

In this paper, the biomechanical properties of the entire human aorta are characterized *in-vivo*, using an MRI/FEA framework. A physiologically based anisotropic hyperelastic constitutive law is presented, that accounts for the individual contributions of elastin, collagen and SMCs within the arterial wall, while making use of a constrained mixture-based approach. Additionally, a framework for generating subject-specific FE models directly from MRI/CT scans is presented. The pressure-area relationship (derived in Part I) throughout the entire cardiac cycle is captured at 10 planes from the proximal ascending to distal abdominal aorta using the novel constitutive law.

2.1 Physiologically based aortic constitutive law

In this section we outline the key equations that describe of the stress response of the material to deformation. The constitutive model is decomposed into isotropic and anisotropic parts; the isotropic portion is used to model the arterial groundmatrix, while the anisotropic part is further divided into separate stress components that describe elastin, collagen and SMCs. Additionally, we model the aortic wall as compressible [29].

We employ a rule of mixtures approach where each component of the wall undergoes the same strain, but the stresses are additive, and the sum of constituent densities (V_α^f) equals unity, which yields

$$\boldsymbol{\sigma} = \boldsymbol{\sigma}_{\mathrm{col}} + \boldsymbol{\sigma}_{\mathrm{ela}} + \boldsymbol{\sigma}_{\mathrm{smc}} + \boldsymbol{\sigma}_{\mathrm{mat}} \tag{1}$$

$$\sum V_\alpha^f = 1 \tag{2}$$

We employ a bilinear strain energy function to capture the strain stiffening behaviour of fibrillar collagen under tension

$$\boldsymbol{\sigma}_{\mathrm{col}} = V_{col}^f * \begin{cases} 0 & \rightarrow 0 > \varepsilon \\ (k_1\varepsilon) * (\boldsymbol{a}_{col} \otimes \boldsymbol{a}_{col}) & \rightarrow 0 < \varepsilon < \varepsilon_t \\ (k_1\varepsilon + k_2(\varepsilon - \varepsilon_t)) * (\boldsymbol{a}_{col} \otimes \boldsymbol{a}_{col}) & \rightarrow 0 < \varepsilon > \varepsilon_t \end{cases} \tag{3}$$

where V_{col}^{f} is the volume fraction of collagen in the wall, k_1 is the initial stiffness of collagen, k_2 is the secondary stiffness of collagen, ε_t is the transition strain and $\boldsymbol{a}_{col}$ denotes the direction of collagen fibres in the reference configuration with respect to the circumferential axis of the artery.

Elastin fibres may also contribute to the anisotropy of the vessel with a mean directionality defined by $\boldsymbol{a}_{ela}$. The elastin fibres also exhibit a constant pre-stretch and stiffness and to allow contraction of the vessel such that the stress is

$$\boldsymbol{\sigma}_{ela} = V_{ela}^{f} * \left(\left(\sqrt{I_{4e}} - 1 + \lambda_e\right) * k_e\right) * (\boldsymbol{a}_{ela} \otimes \boldsymbol{a}_{ela}). \tag{4}$$

The model parameter λ_e is the pre-stretch of the elastin component in the initial undeformed configuration. V_{ela}^{f} is the volume fraction of elastin in the wall, and k_e is the stiffness of elastin.

We also incorporate the active component of the wall as represented by σ_{smc}. The contractile stress generated by a single SMC (σ_{act}) is held constant at 25kPa [30]. SMCs also contribute to the anisotropy of the vessel through $\boldsymbol{a}_{smc}$

$$\boldsymbol{\sigma}_{smc} = V_{smc}^{f} * \left(\sigma_{act} * (\boldsymbol{a}_{smc} \otimes \boldsymbol{a}_{smc})\right) \tag{5}$$

where V_{smc}^{f} is the volume fraction of SMCs in the wall, σ_{act} is the active stress of an individual SMC and $\boldsymbol{a}_{smc}$ denotes the direction of SMCs in the reference configuration. Finally, the stress in the isotropic groundmatrix can be defined as

$$\boldsymbol{\sigma}_{mat} = V_{mat}^{f} * \left(\frac{\mu_0}{J^{\frac{2}{3}}}\left(\bar{\mathbf{B}} - \frac{1}{3}\bar{I}_1\mathbf{I}\right) + \frac{2J}{D_1}(J-1)\right) \tag{6}$$

Where V_{mat}^{f} is the volume fraction of matrix in the wall, μ_0 is the shear modulus and D_1 is related to the bulk modulus of the groundmatrix.

2.2 Experimental/clinical motivation for constitutive model

The following three experimental/clinical observations are used to motivate the bespoke arterial constitutive law presented in the previous section.

As illustrated in the schematic in Figure 1, our MRI measurements presented in Part I reveal a bi-linear pressure-area curve in the physiological pressure range (PPR), with a high compliance regime (HCR) transitioning to a low compliance regime (LCR) at an identifiable transition pressure and area (P_t, A_t).

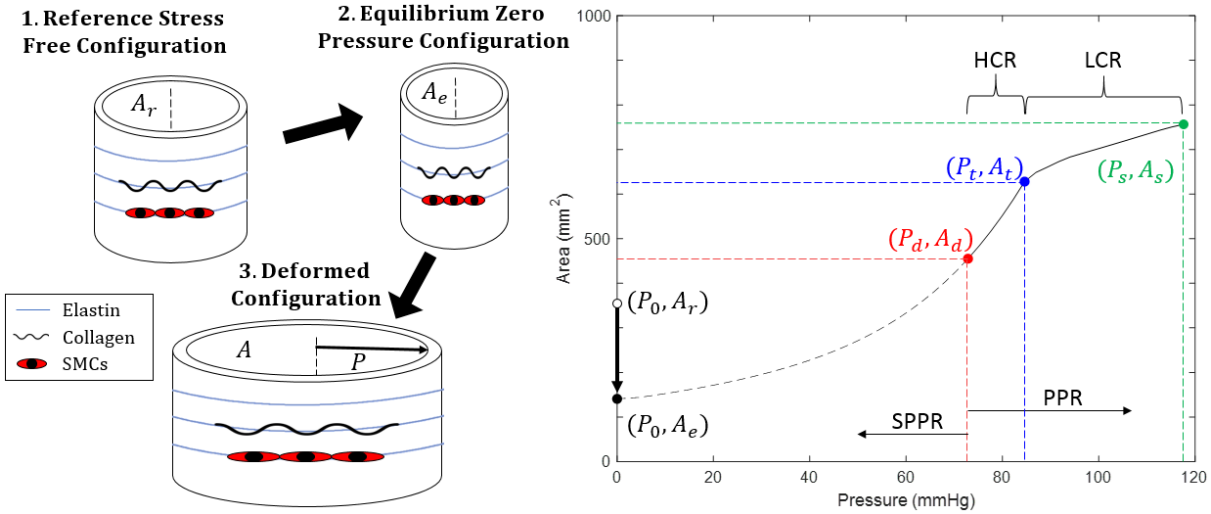

Figure 1: Schematic of modelling framework for simulation of in-vivo aorta behaviour. 1. A reference stress-free configuration is constructed with an area A_r. 2. An equilibrium zero-pressure configuration is computed, whereby the cross-sectional area of the vessel reduces to A_e, such that the internal tensile circumferential stress due to elastin pre-stretch and SMC contractility is in equilibrium with the compressive circumferential stress generated in the matrix. 3.) The lumen pressure is increased from zero up to the end systolic value (117 mmHg). The pressure increases through a sub-physiological pressure regime (SPPR). At the start-diastolic pressure, P_d, (73 mmHg) the computed lumen area is denoted A_d. The pressure is then increased through the physiological pressure range (PPR) up to the end-systolic value, P_s (117 mmHg), at which point the computed area is denoted A_s. As illustrated in the pressure-area curve above, based on the MRI measurements of Part I, the PPR is characterised by a high compliance regime (HCR) up to a transition pressure, P_t, followed by a low compliance regime (LCR) up to the end of systole.

Furthermore, a study by Swanson and Clark [31] reveals that the aortic lumen area at zero pressure (A_r) is ~30% lower than the end-diastolic lumen area (A_d). A computational model must predict the deformation from the zero-pressure aortic configuration (A_r) up to the maximum systolic pressure configuration (A_s), including the transition from HCR to LCR in the PPR. To consider the ability of purely elastic models to capture such behaviour, we simulate the expansion of an idealised cylindrical artery with undeformed lumen area A_r with the lumen pressure increasing from zero to 120 mmHg. Firstly, we consider a standard Yeoh hyperelastic model. As shown in Figure 2(a) a good fit for the expected pressure-area curve is obtained. However, the required sigmoidal shape of the associated stress-strain curve (Figure 2(b)) is not representative of the expected bi-linear strain stiffening that has been widely reported for the aorta. In Figure 2(c) we consider the behaviour of our bi-linear collagen and Neo-Hookean matrix model (equations 3 and 6) without the inclusion of elastin or SMCs. A reasonable fit is achieved for the pressure-area curve only if an extremely high transition strain ($\varepsilon_t > 60\%$) is specified for the collagen model. As shown in Figure 2(d), this requires the specification of a stress-strain relationship that is not representative of the aorta. In

summary, Figures 2(a-d) demonstrate that non-contractile elastic models can only predict the pressure-area behaviour of the aorta if an incorrect stress-strain relationship is used. We next consider aortic contractility through the addition of pre-stretched elastin to the model (equation 4). In this case, we choose a starting reference lumen area $A_r = 485\ \mathrm{mm}^2$. A preliminary analysis step is implemented in which the artery contracts until the tensile stress of the pre-stretched elastin is in equilibrium with the compressive stress of the groundmatrix (collagen fibres shorten in such a deformation and therefore do not contribute to the stress state at this point of the analysis). Elastin and matrix properties (λ_e, k_e and μ) are chosen so that this equilibrium lumen area is close to the expected zero-pressure area ($A_e \approx A_0$). Next, starting from this equilibrium configuration (A_e), the lumen pressure is then increased from zero to 120 mmHg and the resultant pressure-area curve is computed (Figure 2(e)). This model provides an accurate representation of clinical/experimental pressure-area data while the corresponding stress-strain behaviour is in the experimentally reported range. The contractility due to the elastin results in a collagen induced stiffness increase at a nominal strain of ~0.4, as reported in the literature. Finally, inclusion of the SMC contribution (equation 5) adds further internal contractility. Again, an accurate representation of the pressure-area curve is achieved (Figure 2(g)) while the corresponding stress-strain curve is within the expected experimental range (Figure 2(h)).

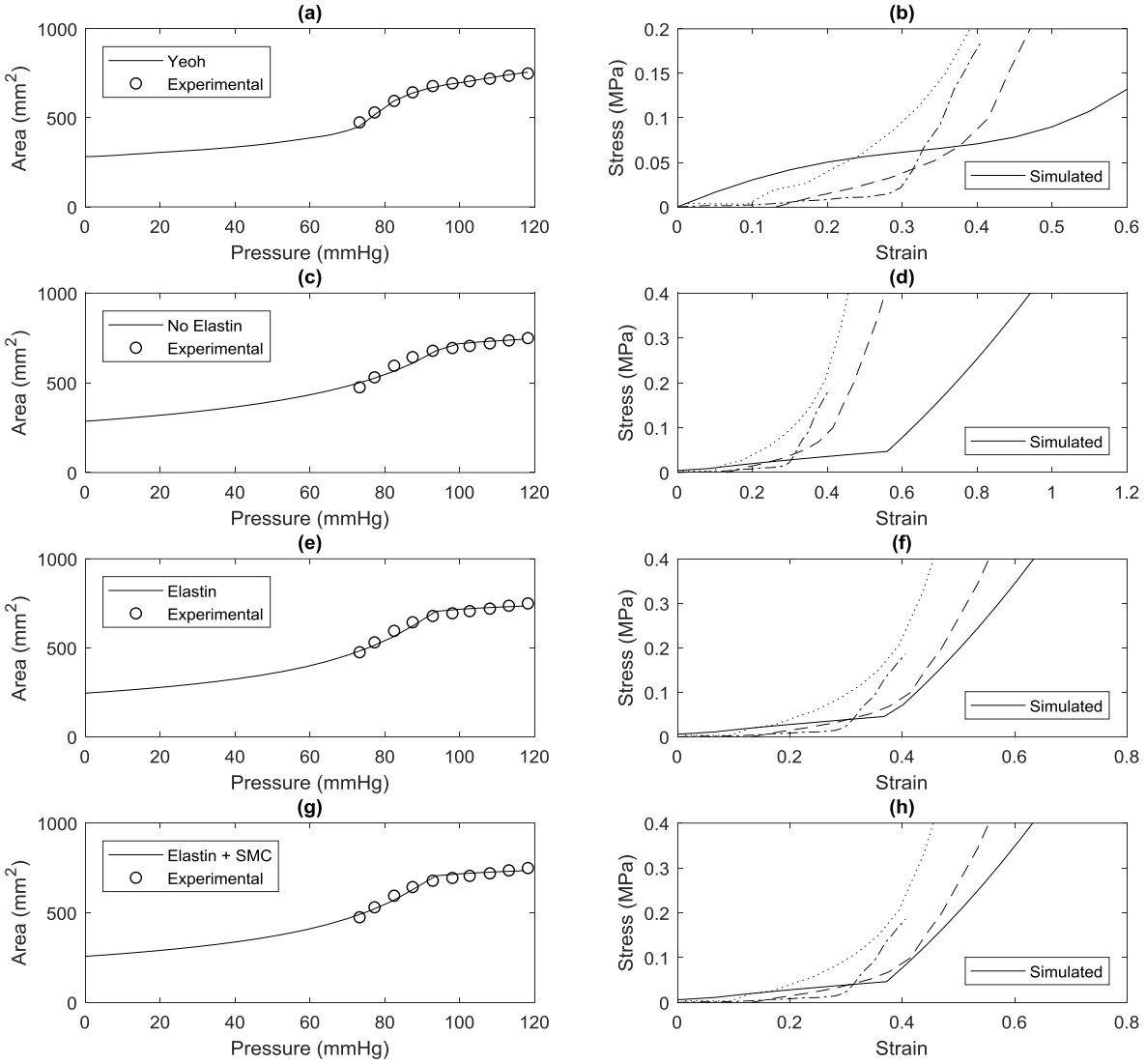

Figure 2: Assessment of modelling strategies to simulate the bi-linear pressure-area curve measured in the PPR *in-vivo* using dual-VENC 4D Flow MRI framework (Part I). (a) Internal contractility is ignored, and the vessel is simply inflated from the reference stress free configuration (A_r). A sigmoidal shaped bi-concave Yeoh hyperelastic material model can be used to fit the pressure-area curve. However, as shown in (b), the tensile stress-strain relationship of this model does not resemble reported experimental data for arterial tissue (dashed=[32]; dotted=(Khanafer et al.,, 2013); dashed/dotted=[34]). (c) shows the pressure-area curve computed using the bi-linear collagen (equation 3) and Neo-Hookean matrix (equation 6) components of the proposed model *without* the inclusion of internal contractility due to elastin or smooth muscle. A reasonable fit can be achieved for the pressure-area curve. However, as shown in (d), an extremely high transition strain (ε_t > 60%) must be specified for the collagen model, and as such, the corresponding stress-strain relationship is not representative of reported experimental data. (e) Internal contractility is next implemented by addition of elastin pre-stretch (equation 4) to the model. A reasonable prediction for the pressure-area curve is obtained, and, as shown in (f), the corresponding tensile stress-strain relationship is now within the experimentally reported range. (g & h) show that similarly accurate and physiologically relevant predictions can also be achieved by the further addition of SMC contractility (equation 5) to the model.

Further evidence of the importance of the elastin pre-stretch component of our model is provided by the recent experiments of Gabriela-Espinosa [35] (Figure 3(a)) whereby pressure-diameter curves for excised rat arteries are measured. The contribution of elastin is then removed by treatment with elastase, which results in an increase in the zero-pressure diameter from 379μm to 473μm, and an increase in compliance across the range of applied lumen pressures. Others have also observed this phenomenon in both canine [36], and murine arteries [37], [38]. As shown in Figure 3(b), our computational model accurately predicts the experimentally observed alteration in the pressure-diameter curve upon the removal of the pre-stretched elastin contribution from the model. This demonstrates that the proposed mechanism of elastin generated internal tension, and its relative contribution to observed non-linear arterial compliance, is physiologically appropriate. Regarding the influence of SMC contractility on aortic biomechanics, Figure 3(c) reproduces the results of an experimental study performed on canine aortae by Barra [39]. The measured circumferential stress-strain relationship for untreated excised tissue is compared to the stress-strain relationship following SMC activation by phenylephrine. SMC activation results in a ~25-40% increase in stress over the applied strain range. Similar trends have also been reported for middle cerebral arteries of rats [40]. As shown in Figure 3(d), our model replicates the experimentally observed contribution of SMC active contractility and suggests that the value of σ_{act} in the range from 25-50 kPa [30] is physiologically appropriate for aortic tissue.

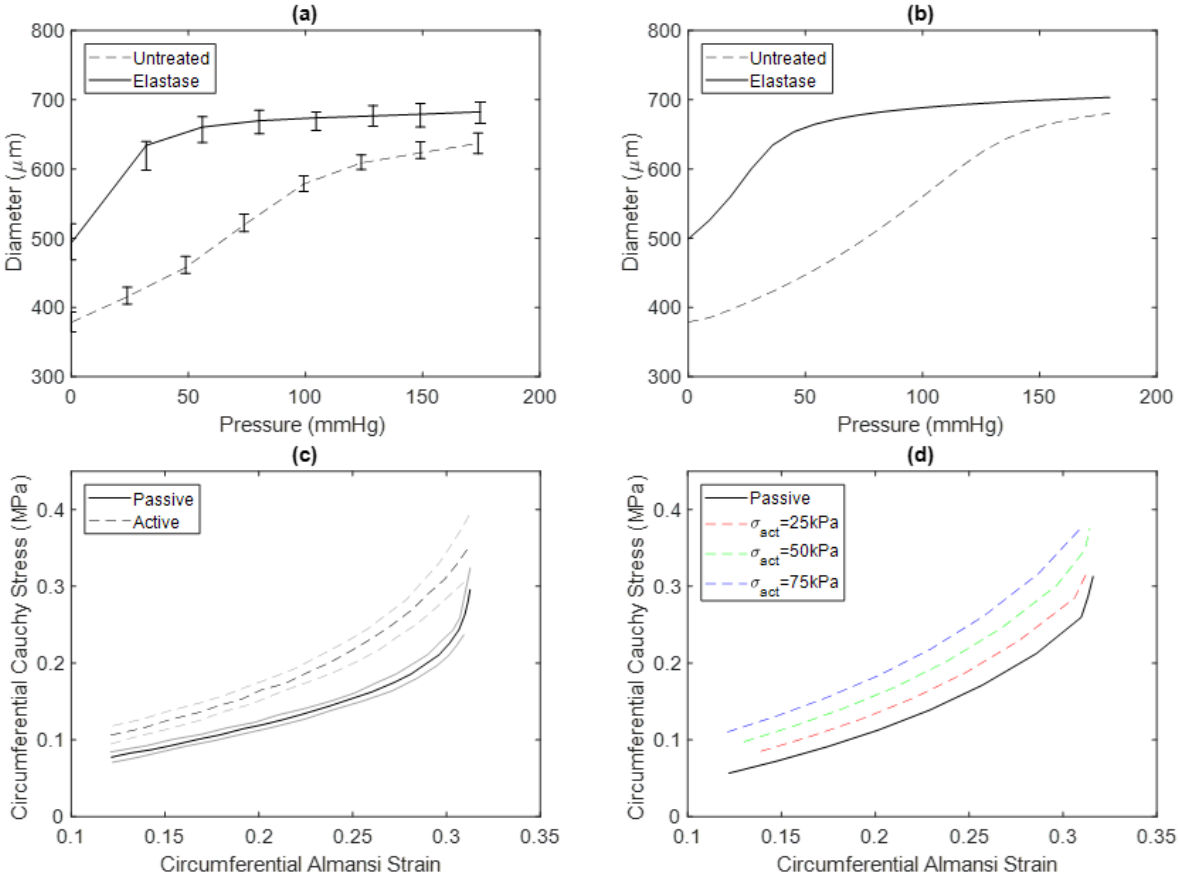

Figure 3: (a) Experimental data reported by Gabriela-Espinosa [35] are reproduced, demonstrating that the digestion of elastin from excised aortae (using elastase treatment) leads to an increase in the observed diameter at zero pressure. Subsequent increases in lumen pressure demonstrate a significant difference between the pressure-area curve between untreated aortae and elastase treated aortae. (b) Computational prediction of the experimental data of Gabriela-Espinosa [35] using our novel constitutive law (equations 1-6). Here we simulate elastase treatment by removing the contribution of the pre-stretched elastin (equation 4). (c) Experimental data reported by Barra [39] are reproduced, demonstrating that activation of SMCs in excised aortae (using phenylephrine) leads to a ~25-40% increase in stress over the applied strain range. (d) Computational prediction of the experimental data of Barra [39] using our novel constitutive law (equations 1-6). An active SMC stress of σ_{act}=25-50 kPa provides a reasonably accurate prediction of the experimental data.

2.3 Model parameter sensitivity study

As outlined in the previous section, our model is physically based, with each component motivated by physiological observations of artery pressure-area and stress-strain curves. This allows for a physiologically based calibration of the model, rather than a black-box fitting of model parameters. For example, the increased collagen stiffness parameter (k_2) is determined through observation of the LCR region of the pressure-area curve (see Figure 1), whereas the equilibrium zero-pressure lumen area, A_e is governed by the values of elastin stiffness (k_e) and pre-stretch (λ_e) relative to the value of the matrix stiffness (μ). Notwithstanding the

physiological interpretation of each model parameter, it is useful to consider the sensitivity of the artery pressure-area curve to each parameter, as presented in Figure 4. In terms of collagen parameters, k_1 and k_2 influence the HCR and LCR region, respectively, as expected, while ε_t strongly influences the transition pressure from HCR to LCR. Collagen parameters do not influence the behaviour in the sub-physiological pressure range (SPPR), as in its highly wavy shortened state the mechanical contribution of collagen is assumed to be negligible [41]. The elastin parameters, k_e and λ_e, and the matrix stiffness, μ, influence the pressure-area curve in the SPPR and in the HCR (with the collagen contribution dominating the slope of the pressure-area curve in the LCR). λ_e and μ strongly influences the zero-pressure equilibrium area A_e. The bulk modulus of the matrix is assumed to be slightly compressible [29] and does not strongly influence the pressure-area curve. Finally, as expected, an increase in SMC contractility (σ_{act}) results in a reduction in the zero-pressure equilibrium area A_e and an increase in the transition area P_t.

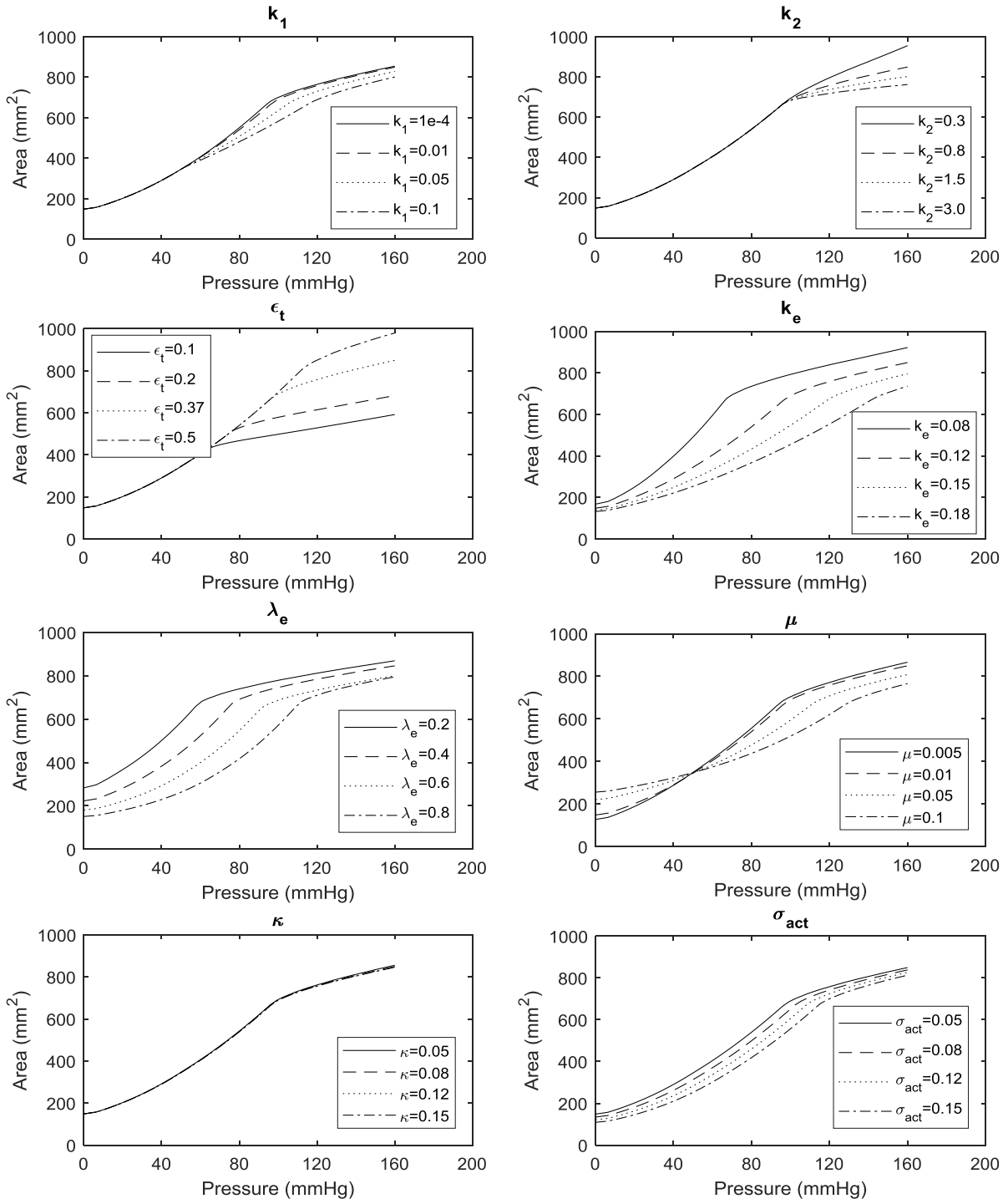

Figure 4: Parametric study to investigate the sensitivity of the computed pressure-area curve to model parameters. Unless otherwise indicated, the following baseline parameter values are used: (Collagen component) k_1 = 0.01 MPa, k_2 = 0.8 MPa, ε_t = 0.37; (Elastin component) k_e = 0.12 MPa, λ_e = 0.4; (Matrix component) μ=0.01 MPa, κ = 0.08 MPa; (SMC component) σ_{act} = 0 kPa.

We dedicate the remainder of this paper to the analysis of the subject-specific MRI dataset uncovered in Part I. In keeping with the physiological motivation and interpretation of our model, we assume that fundamental material properties that describe collagen (k_1, k_2) and elastin (k_e, λ_e) do not change as a function of location in the aorta. Rather, we assume that volume fractions of collagen (V_{col}^f), elastin (V_{ela}^f), smooth muscle (V_{smc}^f) and matrix (V_{mat}^f) may spatially vary [23], [25], [26]. Therefore, the subject-specific model is primarily calibrated by altering V_{col}^f, V_{ela}^f and V_{smc}^f.

In Figure 5 we illustrate the sensitivity of the pressure-area curve to changes in artery composition. As expected, an increase in V_{col}^f increases the stiffness of the aorta in the LCR but does not affect the stiffness in the HCR, as the collagen here is crimped. An increase in V_{col}^f also results in a decrease in the A_e through the volume conservation relationship described in equation 2 (as V_{col}^f increases, V_{mat}^f must decrease and the elastin contraction leads to a greater matrix compression. Note: collagen does not contribute mechanically in compression). An increase in V_{ela}^f also results in a decrease in A_e, due to a greater volume of contractile elastin compressing within a lesser volume of matrix. Increasing V_{ela}^f alters the stiffness of the aorta in both the SPPR and the HCR but has no effect on the stiffness in the LCR as once ε_t is exceeded the secondary collagen stiffness dominates the behaviour of the material. Increasing the V_{smc}^f does not influence the stiffness in either the HCR or the LCR, as effectively the same material behaviour is achieved as decreasing the matrix stiffness (μ), (see Figure 4). As a result, an increase in V_{smc}^f, results in a decrease in A_e, and an increase in $\mathrm{P_t}$.

In addition to spatial variation in volume fractions of the constituent components, we also consider spatial variation in the collagen transition strain (ε_t). This assumption is based on the reported histological observations that the waviness of collagen in the aorta decreases distally [42]. The waviness of collagen fibers directly effects the strain at which increased stiffness occurs. We also consider spatial variations in the stiffness of the matrix based on reported data that the makeup of GAGs in the aorta differs proximally versus distally [43].

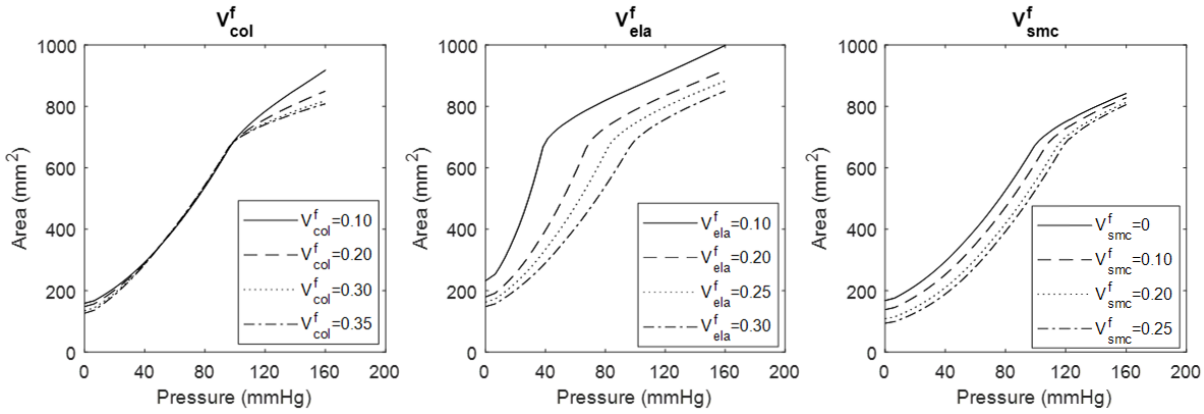

Figure 5: Parametric study to investigate the sensitivity of computed PA curves to the volume fractions of collagen (V^f_{col}), elastin (V^f_{ela}), and smooth muscle cells (V^f_{smc}).

2.4 Construction of subject-specific finite element model

The following section describes the methodology surrounding the generation of a subject-specific FE model, directly from the MRI data obtained in Paper I using a custom-built MATLAB (R2017b, MathWorks Inc., Natick, MA, USA) framework.

Firstly, the aortic centreline (Figure 6(a)) and the lumen boundary points corresponding to the diastolic timepoint in the cardiac cycle, for each of the 10 planes analysed (Figure 6(b)), were used to sweep a surface mesh along the main trunk of the aorta. All major branch vessels were added to the main trunk including the innominate artery, left common carotid artery, left subclavian artery, coeliac artery, superior and inferior mesenteric arteries, left and right renal arteries and left and right common iliac arteries, to form the full aortic internal and external surface models (Figure 6(c)). Cadaveric aortic wall thickness data from Concannon [26] is highlighted as a function of aortic location in Figure 6(d), which can be used to specify the element specific offset distance from the internal surface elements (green) to the external surface elements (red) in Figure 6(e). Finally, the transformation of both sets of surface elements into 3D continuum elements, yields the final aortic model shown in Figure 6(f).

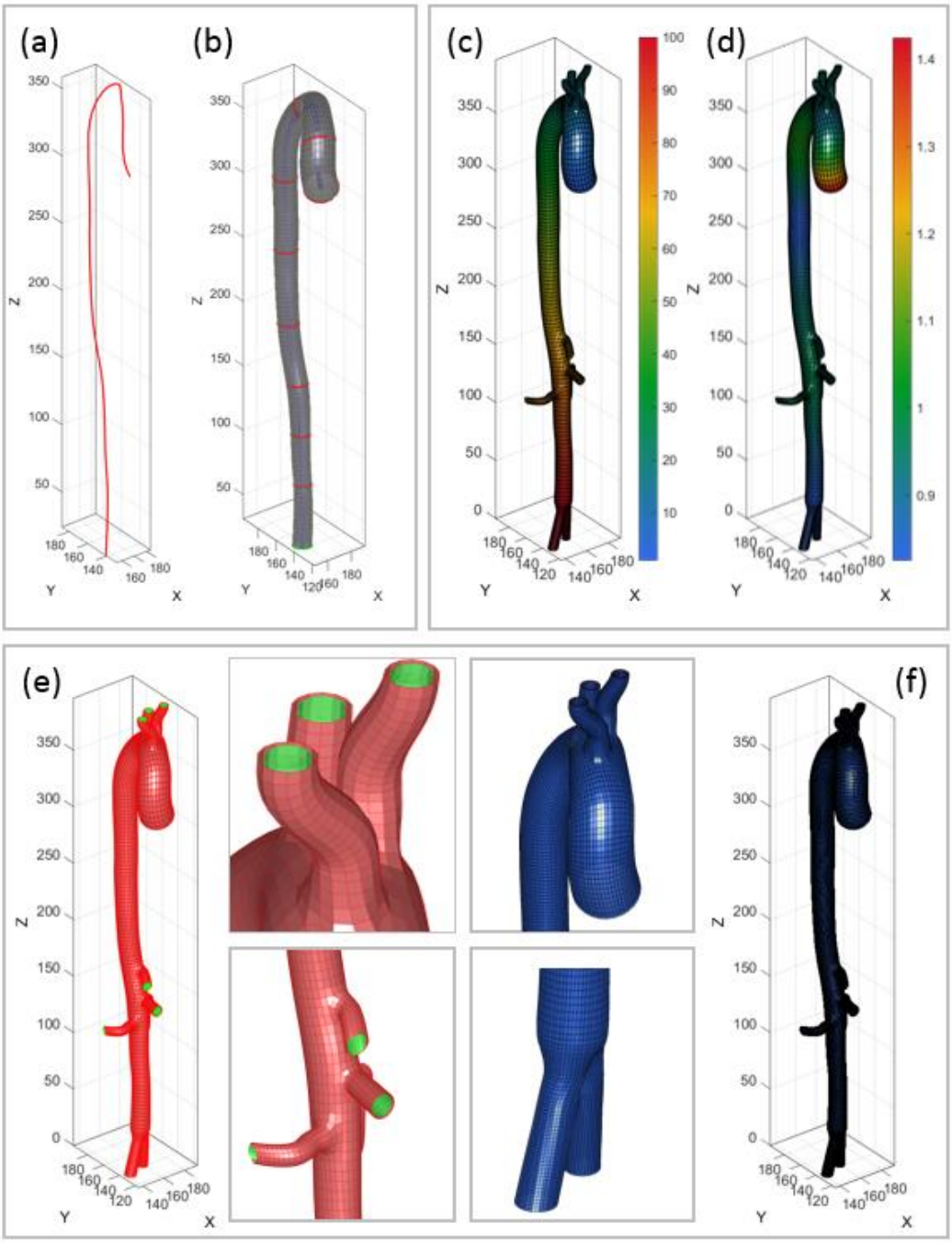

Figure 6: Finite element mesh generation. (a) aortic centreline and (b) plane profiles used for sweeping the internal surface mesh, (c) major branching vessels along the aorta (d), spatially varying aortic wall thickness, (e) offset of internal surface elements by the wall thickness to generate the external surface mesh (red), and (f) hexahedral splitting to generate C3D8 continuum elements.

2.5 Simulation of subject-specific aortic biomechanical behaviour

A discrete fiber orientation based on the aortic centreline and internal lumen surface of the aorta was prescribed to ensure the circumferential orientation of each element was defined. The pre-stretched elastin is incorporated in the subject-specific FE model in the same manner

described previously, through an initial contraction step resulting in a new equilibrium configuration, in this case for the entire aorta. The subject-specific diastolic pressure load of 73 mmHg was then applied to the internal lumen surface, followed by a pulse pressure wave based on the measurements outlined in Part I. A linear interpolation of material parameters is assumed between each of the 10 calibrated sections. The final simulated versus experimental pressure-area curve fits are shown in Figure 7.

3 Results

Figure 7 shows the computed pressure-area curves at the 10 planes along the length of the subject-specific aorta. At each section, the volume fractions of collagen (V_{col}^{f}), elastin (V_{ela}^{f}), and SMCs (V_{smc}^{f}) within the wall, in addition to the isotropic groundmatrix shear modulus (μ) and the transition strain (ε_t) are adjusted so that the MRI measured data at each section is accurately predicted. Furthermore, at each plane, the contraction of the aorta due to the pre-stretch of elastin results in a 31-49% reduction from the reference configuration to the new equilibrated configuration, accurately reflecting the range reported by the experiments of [35], [36], and [38].

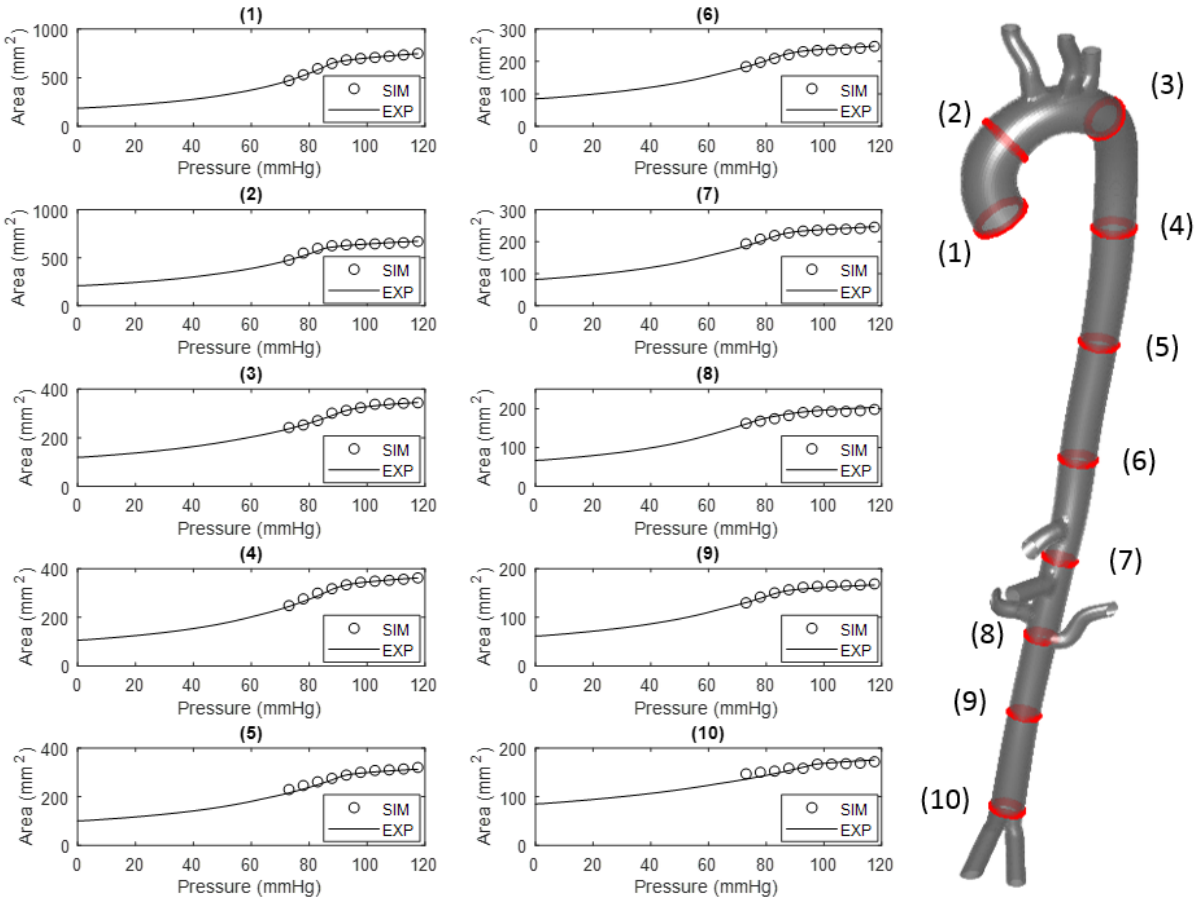

Figure 7: Comparison of computed pressure-area curves (SIM) with MRI measurements at 10 planes along the length of the aorta. Computed data in the SPPR (including the contracted area A_e at zero pressure) is shown, in addition to the bi-linear pressure-area predictions in the PPR. The model is shown to accurately capture the spatially varying MRI data simply by calibrating the spatially varying volume fractions of the constituent phases (V^f_{col}, V^f_{ela}, V^f_{smc}), the transition strain of the collagen (reflecting the waviness of the collagen), and the matrix shear modulus (reflecting spatially varying GAG content). All other model parameters are uniform throughout the aorta.

The time dependence in circumferential tangent stiffness ($\delta\sigma_c/\,\delta\varepsilon_c$) due to the pressure wave of a single cardiac cycle is shown in Figure 8 and reflects the high and low compliance regimes in the pressure-area relationship along the entire aorta.

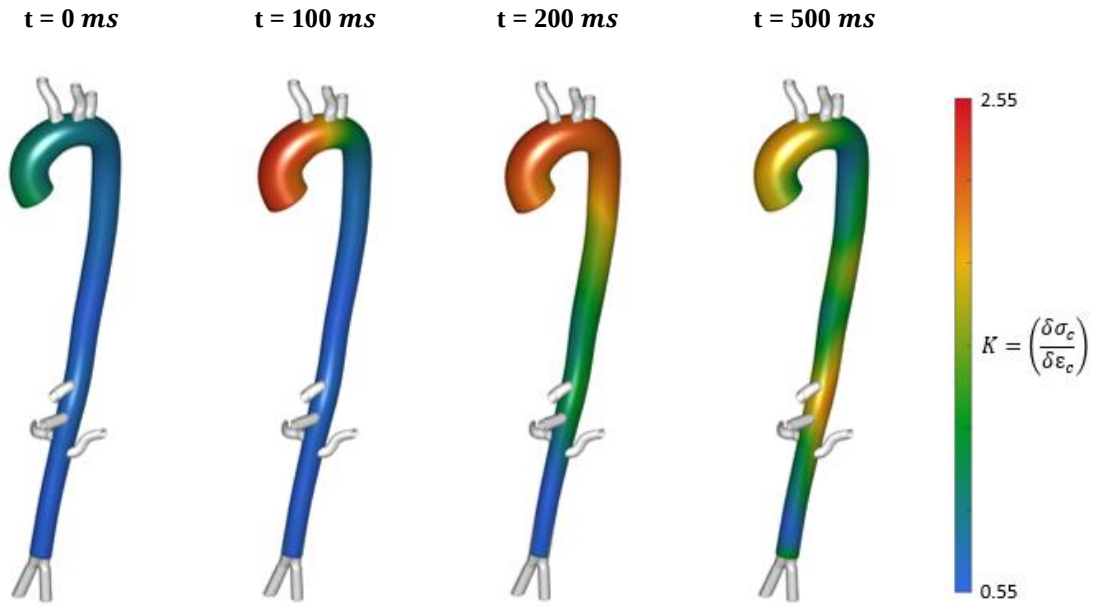

Figure 8: Computed effective circumferential tangent stiffness, *K* (MPa) throughout the aorta at four different time-points during the cardiac cycle (t=0 ms, t=100 ms, t=200 ms, and t=500 ms). The complex spatial and temporal changes in effective material tangent stiffness are clearly illustrated.

Figure 9 shows the FE model predictions of elastin volume fraction (V_{ela}^{f}) along the length of the aorta. The model predicts that V_{ela}^{f} decreases from a maximum value of 35% at Plane 1 (proximal aorta) to a minimum value of 19% at Plane 10 (distal aorta). This finding is strongly supported by the histological data uncovered in Concannon [26], and is superimposed in Figure 9 for comparison.

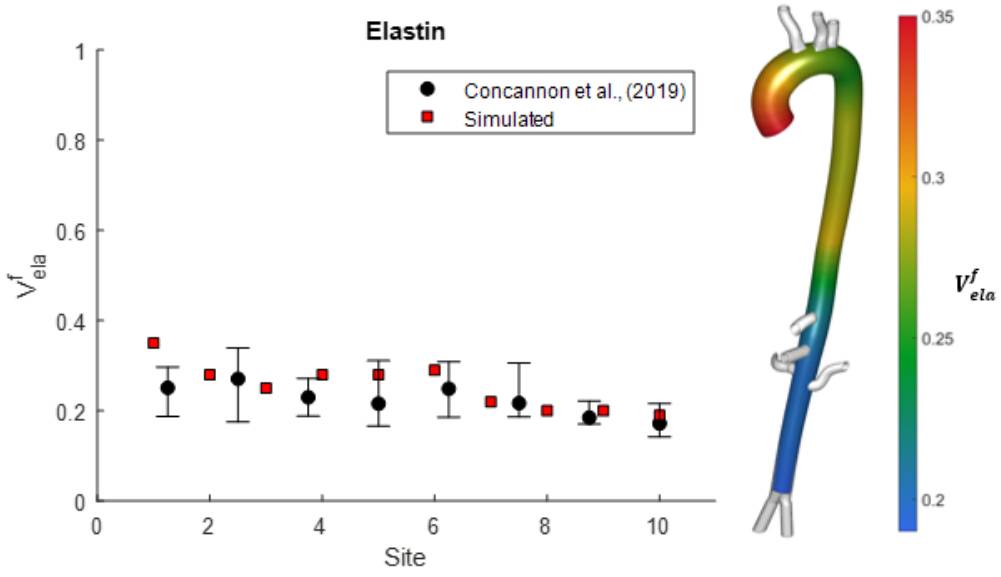

Figure 9: Computed elastin volume fractions (V_{ela}^{f}) as a function of position (anatomical site – see Figure 5.5) in the aortic wall (red squares). Corresponding elastin content measured in the experimental histology study (Concannon [26]) are superimposed for comparison (black circles).

Figure 10 shows the FE model predictions of collagen volume fraction (V_{col}^{f}) along the length of the aorta. The model predicts that V_{col}^{f} increases from a minimum value of 20% at Plane 1 (proximal aorta) to a maximum value of 50% at Plane 10 (distal aorta). This finding is strongly supported by the histological data uncovered in Concannon [26], and is superimposed in Figure 10 for comparison.

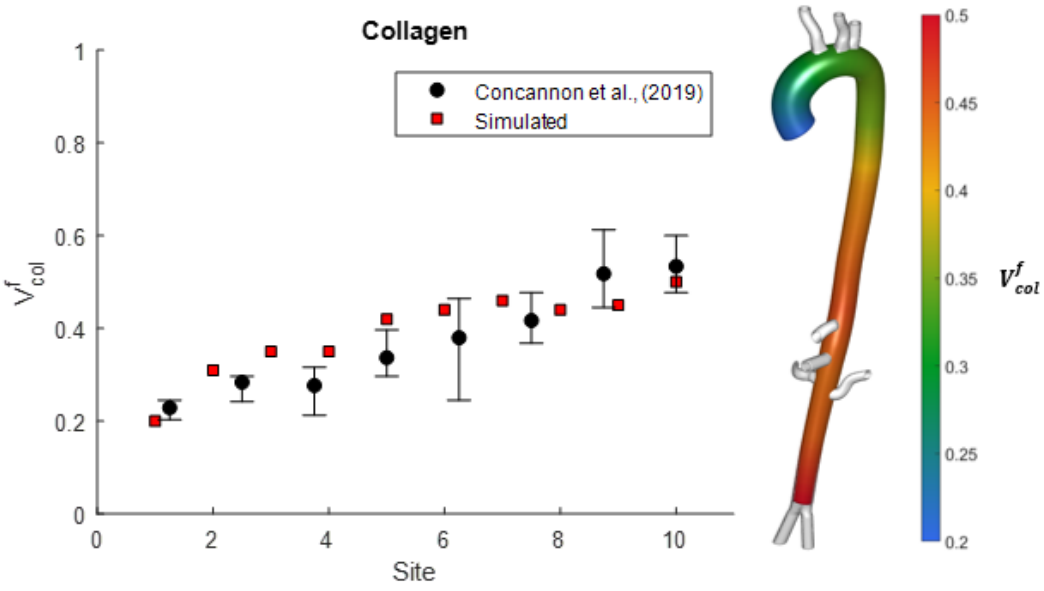

Figure 10: Computed collagen volume fractions (V_{col}^{f}) as a function of position (anatomical site – see Figure 5.5) in the aortic wall (red squares). Corresponding collagen content measured in the experimental histology study (Concannon [26]) are superimposed for comparison (black circles).

The transition strain is plotted as a function of aortic location in Figure 11. It is observed that in order to fit the regional *in-vivo* pressure-area curves that the transition strain decreases from 0.38 in the proximal ascending aorta to 0.15 in the distal abdominal segment. This result is in agreement with the *in-vitro* work of Zeinali-Davarani [42] who found that the degree of collagen undulation observed under multi-photon microscopy also decreased between the proximal and distal aorta in pigs. The waviness (S) is defined as the direct distance between the end points of a fiber (L) divided by the actual length of fiber (l) (i.e. S=1 for a perfectly straight fiber, whereas S<1 for a wavy fibre). A statistically significant difference was found in the waviness of collagen fibers between the thoracic (S=0.77±0.09) and abdominal (S=0.37±0.02) aorta.

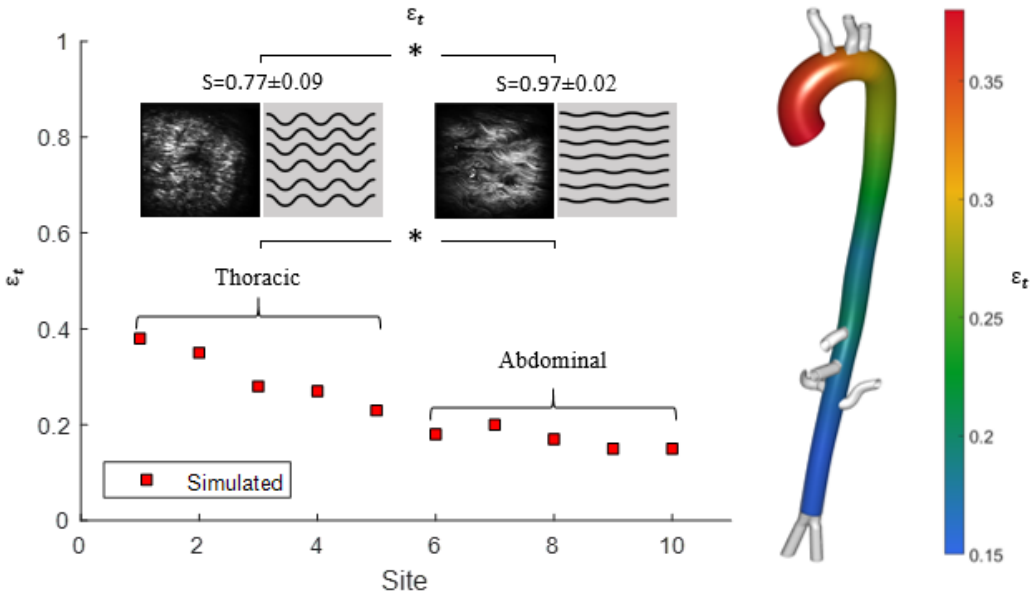

Figure 11: Computed collagen transition strain (ε_t) as a function of position (anatomical site – see Figure 5.5) in the aortic wall (red squares). The parameter ε_t represents the waviness of the collagen, with a high transition strain indicating a high level of waviness. Experimental histological measurements of collagen waviness (characterised by the waviness factor S) in thoracic and abdominal porcine aortas are shown for comparison. The statistically significant difference ($p < 0.05$) between the two experimental groups is also evident in our computational results.

Finally, in Figure 12 we show the FE model predictions of SMC volume fraction (V_{smc}^f) along the length of the aorta. The model predicts that V_{smc}^f increases from a minimum value of 20% at Plane 1 (proximal aorta) to a maximum value of 27% at Plane 10 (distal aorta). This finding is strongly supported by the histological data uncovered in Concannon [26], and is superimposed in Figure 12 for comparison.

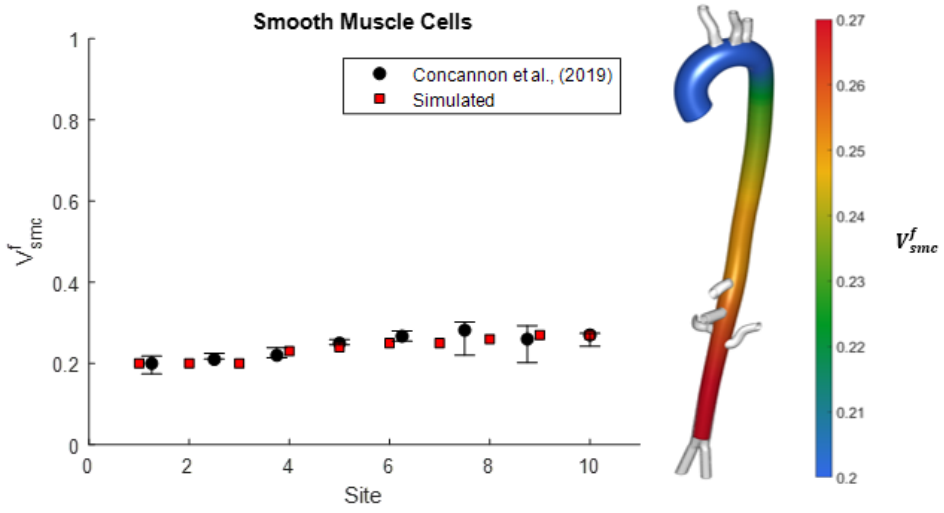

Figure 12: Computed SMC volume fractions (V_{smc}^f) as a function of position (anatomical site – see Figure 5.5) in the aortic wall (red squares). Corresponding SMC content measured in the experimental histology study (Concannon et al., 2019) are superimposed for comparison (black circles).

4 Discussion

This paper develops a subject-specific MRI/FEA framework to uncover the biomechanisms underlying the spatially varying non-linear aortic compliance measured *in-vivo* in Part I. Several key findings emerge from the work:

(i) Internal vessel contractility, due to pre-stretched elastin fibres and actively generated smooth muscle cell stress, must be incorporated into the arterial constitutive law, along with collagen strain stiffening, in order to accurately predict the non-linear pressure-area relationship uncovered by our MRI investigation.

(ii) Modelling of elastin and smooth muscle contractility allows for the identification of the reference vessel configuration at zero-lumen pressure. This modelling approach is also shown to capture the key features of elastin and SMC knockout experiments.

(iii) Incorporation of elastin and SMC contractility is critical for the accurate prediction of the physiological lumen pressure at which the aorta transitions from a high-compliance regime to a low-compliance regime due to collagen strain stiffening.

(iv) Volume fractions of the constituent components of the aortic material model (i.e. non-linear elastic collagen, pre-stretched elastin, and contractile smooth muscle cells) were computed throughout the subject-specific aortic FE model so that the *in-silico* pressure-area curves accurately predict the corresponding MRI data at 10 separate anatomical locations. This leads to the prediction that collagen and smooth muscle volume fractions increase distally, while elastin volume fraction decreases distally. This finding is supported by the histological analyses presented in Concannon [26].

(v) The model parameter that sets the strain at which collagen transitions from low- to high-stiffness is computed to be lower in the abdominal aorta. This model prediction supports the histological finding that collagen waviness is lower in this region.

It has been shown that the digestion of elastin significantly increases the zero-pressure vessel diameter and alters the pressure-area relationship in arteries over a range of applied physiological lumen pressures [35], [38]. The inclusion of a pre-stretched linear elastic elastin component in our model accurately replicates the experimental observations of [35]. In our modelling approach the artery configuration at zero-pressure is computed whereby the pre-strained elastin reduces the vessel diameter until the elastin tensile stress is in equilibrium with the compressive stresses in the groundmatrix. The subsequent application of a lumen pressure within the physiological range leads to the accurate prediction of the experimentally measured pressure-area curve. Our model also includes active contractility of SMCs

component. The active SMC stress ($\sigma_{act} = 25$ kPa) determined by McGarry [30] for single SMCs seeded on arrays of micro-pillars leads to a reasonable prediction of the experimentally observed increase in aortic wall stress due to phenylephrine induced SMC contractility [39], [40]. Future developments of the SMC component of the model should include descriptions of the active contractility of SMCs in the aortic wall could include Hill-type tension-strain rate formulations and kinetic formulations for dynamic intra-cellular remodelling of stress fibres [44]–[47]. Micromechanical modelling approaches should also be developed for arterial tissue to analyse the interaction between cells and the surrounding ECM [48], [49].

The computation of the contracted zero-pressure artery configuration with a lumen area that is ~30-50% lower than the undeformed stress-free configuration due to elastin pre-strain and SMC active contractility is a key component of our subject-specific modelling strategy. This approach is physiologically based on experimental observations of lumen area change following the digestion of elastin using elastase and measured stress changes following SMC activation [35], [36], [38]–[40]. We demonstrate that the identification of the contracted configuration prior to the application of the lumen pressure (up to a physiological loading range) is a critical step in order to accurately predict MRI measurements of *in-vivo* non-linear pressure-area relationship (presented in Part I). If elastin and SMC contractility are ignored and the vessel is merely loaded from a '*stress-free*' reference state, a non-physiological stress-strain relationship (e.g. a bi-concave sigmoidal Yeoh hyperelastic formulation, or a non-physiological collagen model that does not strain stiffen until 60% tensile strain) must be used for the artery wall. In contrast, if elastin and SMC contractility are included, the *in-vivo* pressure-area relationship is accurately predicted using a physiologically realistic stress-strain relationship, with collagen strain stiffening at 30-35% tensile strain [32]–[34]. A previous artery modelling strategy by Bols [50], ignores the key contribution of vessel contractility and assumes a polynomial hyperelastic material law. An iterative numerical backwards displacement algorithm was used to estimate zero-pressure stress-free configuration and lumen pressure was directly applied without considering the contracted configuration. A similar approach was implemented by Krishnan [51], with the added simplification of linear elastic material behaviour. Indeed it should be noted that the majority of patient-specific aortic FE models in the literature incorrectly assume that the observed geometry (from MRI or CT imaging) represents a zero-stress state configuration [52]–[60], despite the significant applied lumen pressure loading of the vessel during *in-vivo* imaging.

The incorporation of a bi-linear strain-stiffening collagen constitutive law enables accurate fitting to both the bi-linear *in-vivo* pressure-area data, while providing physiologically realistic uniaxial tension stress-strain behaviour. Within the SPPR and HCR, collagen is crimped, and its mechanical contribution is lower than that of the elastin and groundmatrix. This physical interpretation is validated by the experimental study of Schriefl [61] in which the effects of elastase and collagenase on the mechanical response of aortic tissue is investigated. Elastin is demonstrated to contribute primarily to the effective material stiffness in the low stiffness regime. The removal of elastin using elastase is shown to significantly reduce the material stiffness in the low strain regime. However, removal of elastin does not significantly alter the tangent modulus in the high strain regime, with pronounced (and similar) strain stiffening observed for both treated and untreated samples. However, pronounced strain stiffening is still observed following elastin removal, and the tangent modulus in the high-stiffness regime at high strains is not strongly influenced by elastin removal. Removal of collagen using collagenase does not strongly influence the material stiffness in the low strain regime. However, collagen removal dramatically alters material behaviour in the high strain regime, with strain stiffening being completely eliminated. Our strain stiffening collage model is supported by reported experimental images of collagen deformation in arteries under physiological loading conditions. Collagen fibres are observed to reach a straightened (uncrimped) configuration at an applied lumen pressure of 100 mmHg [62], and at an applied strain of 0.4 [63], [64]. These data strongly support the range of values of transition strains ($\varepsilon_t = 0.18 - 0.35$) and resultant transition pressures ($\mathrm{P_t} = 83 - 93$ mmHg) determined by our MRI/FEA framework.

In order to simulate the spatially varying heterogeneous pressure-area relationships uncovered at 10 aortic planes in *in-vivo* MRI study in Part I, our modelling framework predicts that the volume fraction of collagen increases with distance from the heart (from 20% in the most proximal Plane 1 to 50% in the most distal Plane 10). We also compute that the volume fraction of elastin decreases with distance from the heart (35% proximally to 19% distally), and the SMC volume fraction increases with distance from the heart (20% proximally to 27% distally). These computed spatial variations in collagen, elastin and SMC are strongly supported by histological data. In Concannon [26], histological analyses of excised cadaveric aorta samples reveals that the area fraction of collagen increased from 22 ± 1.6% to 53 ± 5.1%, elastin decreased from 27 ± 4.7% to 17 ± 3.9%, and SMC density increased from 22 ± 2.2% to 27 ± 1.0%. Other studies have also observed that collagen [24],

[65] and SMC concentrations increase distally, while elastin concentration decreases distally [25], [66] in horses, pigs and monkeys. Our modelling framework also computes that the transition strain (ε_t) decreases from 0.38 in the proximal aorta to 0.15 in the abdominal aorta. This finding is supported by the experimental study of [42] who report that collagen in the proximal aorta was more crimped than collagen in the distal aorta in pigs. Furthermore, the experimental biaxial mechanical test data reported [67] and [68] demonstrate that the transition strain is lower in samples extracted from the distal aorta compared to samples from the proximal aorta.

Several computational studies have used the simplifying assumption that the aorta exhibits a single spatially uniform stiffness [69]–[76]. Using our novel MRI/FEA framework, we highlight the inaccuracy of this assumption, and our constitutive law provides a new insight into the link between spatially varying tissue composition and resultant biomechanical function. Furthermore, our framework provides a detailed characterisation of a high compliance regime at low physiological lumen pressures and a low compliance regime at high physiological pressures within a single cardiac cycle. This finding is supported by several *ex-vivo* studies that demonstrate a non-linear compliance over the physiological pressure regime in whales [77], octopus [78], pigs [79] and humans [80], [81].

The generation of a framework for building subject-specific FE models directly from medical imaging data is of significant value to the field of computational biomechanics. Typically, FE meshes are generated through manual segmentation techniques in commercially available software packages such as Mimics (Materialise, Belgium). Such approaches, however, require significant post-processing time, hindering their feasibility as real-time clinical diagnostic tools. Robust alternative approaches to *in-vivo* geometry construction include IVUS and Multislice CT [82], [83] as well as pyFormex software (http://www.pyformex.org) [50]. The custom-built framework developed in this study is open source [84] (now freely available on the MATLAB GIBBON toolbox) and can serve as an *in-silico* test-bed for the testing of novel synthetic materials and stent designs.

This study did not consider the effect of non-circumferentially aligned elastin, collagen and SMCs. O' Connell [85] showed in rats that all three primary medial constituents (elastic lamina, collagen bundles, and smooth muscle cells) have a predominately circumferential orientation. However, collagen fibers have been reported to align at +27.75° and -27.19° to the circumferential direction [86], and in non-symmetric complex distributions which require a von Mises mixture model to capture [26]. Elastin fibers have been reported to

align at -40° [87] and +75° [88] to the circumferential axis, while SMCs have been reported to align between -50° and -20° [89] with respect to the circumferential axis. The constitutive law implemented in the current study can readily be extended to include non-circumferential fibre alignments and non-uniform fibre dispersion distributions. The bi-linear form used in this study to describe the strain stiffening collagen contribution can also readily be extended to include a smooth transition region between the low- and high-stiffness regimes. However, the results of the current study demonstrate that such an additional feature is not required to simulate the distinctly bi-linear shape of the pressure-area curves measured *in-vivo* using our dual-VENC protocol in Part I. Future implementations could also incorporate cohesive zone or element removal damage models to simulate dissection or rupture [90]–[92]. Additionally, our study did not consider the effect of anatomical constraints on aortic deformation, such as the spinal column or lungs. Such additional features can readily be identified from MRI images and incorporated into future model implementations.

In summary, this computational investigation provides new insights into the spatially varying non-linear compliance of the aorta, uncovering the key role of pre-stretched elastin, contractile SMCs and strain stiffening collagen on in vivo biomechanical behaviour. We demonstrate that our subject-specific MRI/FEA framework can predict the spatial vairiation of collagen, elastin and SMC throughout the aorta and can accurately predict the complex spatially varying pressure-area relationship under physiological loading. The subject-specific MRI/FEA framework can potentially be used to guide preoperative planning of aortic surgery, e.g. endovascular or open surgical repair, and aid in the design of next generation patient-specific aortic devices.

6 Acknowledgements

This study was supported by the Irish Research Council (EPSPG_2016_194).

7 Disclosures

None

8 Bibliography

[1] J. P. Vande Geest, M. S. Sacks, and D. A. Vorp, "The effects of aneurysm on the biaxial mechanical behavior of human abdominal aorta.," *J. Biomech.*, vol. 39, no. 7, pp. 1324–34, Jan. 2006.

[2] T. Matsumoto, T. Fukui, T. Tanaka, N. Ikuta, T. Ohashi, K. Kumagai, H. Akimoto, K. Tabayashi, and M. Sato, "Biaxial Tensile Properties of Thoracic Aortic Aneurysm Tissues," *J. Biomech. Sci. Eng.*, vol. 4, no. 4, 2009.

[3] C. Forsell, J. Roy, and T. C. Gasser, "The Quasi-Static Failure Properties of the Abdominal Aortic Aneurysm Wall Estimated by a Mixed Experimental-Numerical Approach," *Ann. Biomed. Eng.*, 2013.

[4] N. Gundiah, A. R. Babu, and L. A. Pruitt, "Effects of elastase and collagenase on the nonlinearity and anisotropy of porcine aorta," *Physiol. Meas.*, vol. 34, no. 12, pp. 1657–1673, Dec. 2013.

[5] C. Reeps, A. Maier, J. Pelisek, F. Härtl, V. Grabher-Meier, W. A. Wall, M. Essler, H.-H. Eckstein, and M. W. Gee, "Measuring and modeling patient-specific distributions of material properties in abdominal aortic aneurysm wall.," *Biomech. Model. Mechanobiol.*, vol. 12, no. 4, pp. 717–33, Aug. 2013.

[6] H. Weisbecker, C. Viertler, D. M. Pierce, and G. A. Holzapfel, "The role of elastin and collagen in the softening behavior of the human thoracic aortic media," 2013.

[7] D. M. Pierce, F. Maier, H. Weisbecker, C. Viertler, P. Verbrugghe, N. Famaey, I. Fourneau, P. Herijgers, and G. A. Holzapfel, "Human thoracic and abdominal aortic aneurysmal tissues: Damage experiments, statistical analysis and constitutive modeling," *J. Mech. Behav. Biomed. Mater.*, vol. 41, pp. 92–107, Jan. 2015.

[8] Z. Teng, J. Feng, Y. Zhang, Y. Huang, M. P. F. Sutcliffe, A. J. Brown, Z. Jing, J. H. Gillard, and Q. Lu, "Layer- and Direction-Specific Material Properties, Extreme Extensibility and Ultimate Material Strength of Human Abdominal Aorta and Aneurysm: A Uniaxial Extension Study," *Ann. Biomed. Eng.*, vol. 43, no. 11, pp. 2745–2759, Nov. 2015.

[9] K. Laksari, D. Shahmirzadi, C. J. Acosta, and E. Konofagou, "Energy-based constitutive modelling of local material properties of canine aortas," *J. R. Soc. Interface*, vol. 3, no. 9, p. 160365, 2016.

[10] N. Choudhury, O. Bouchot, L. Rouleau, D. Tremblay, R. Cartier, J. Butany, R. Mongrain, and R. L. Leask, "Local mechanical and structural properties of healthy and diseased human ascending aorta tissue," 2009.

[11] D. C. Iliopoulos, R. P. Deveja, E. P. Kritharis, D. Perrea, G. D. Sionis, K. Toutouzas, C. Stefanadis, and D. P. Sokolis, "Regional and directional variations in the mechanical properties of ascending thoracic aortic aneurysms," *Med. Eng. Phys.*, vol. 31, no. 1, pp. 1–9, 2009.

[12] S. Pasta, J. A. Phillippi, A. Tsamis, A. D'Amore, G. M. Raffa, M. Pilato, C. Scardulla, S. C. Watkins, W. R. Wagner, T. G. Gleason, and D. A. Vorp, "Constitutive modeling of ascending thoracic aortic aneurysms using microstructural parameters.," *Med. Eng. Phys.*, Dec. 2015.

[13] S. G. Sassani, S. Tsangaris, and D. P. Sokolis, “Layer- and region-specific material characterization of ascending thoracic aortic aneurysms by microstructure-based models,” *J. Biomech.*, vol. 48, no. 14, pp. 3757–3765, 2015.

[14] D. Mohan and J. W. Melvin, “Failure properties of passive human aortic tissue. i-uniaxial tension tests,” 1982.

[15] J. P. Vande Geest, M. S. Sacks, and D. A. Vorp, “Age Dependency of the Biaxial Biomechanical Behavior of Human Abdominal Aorta,” *J. Biomech. Eng.*, vol. 126, no. 6, p. 815, Dec. 2004.

[16] M. L. Raghavan, M. M. Hanaoka, J. A. Kratzberg, M. de L. Higuchi, and E. S. da Silva, “Biomechanical failure properties and microstructural content of ruptured and unruptured abdominal aortic aneurysms,” *J. Biomech.*, vol. 44, no. 13, pp. 2501–2507, Sep. 2011.

[17] P. Hallock and I. C. Benson, “STUDIES ON THE ELASTIC PROPERTIES OF HUMAN ISOLATED AORTA,” *J. Clin. Invest.*, vol. 16, no. 4, pp. 595–602, Jul. 1937.

[18] T. Moriwaki, T. Oie, K. Takamizawa, Y. Murayama, T. Fukuda, S. Omata, K. Kanda, and Y. Nakayama, “Variations in local elastic modulus along the length of the aorta as observed by use of a scanning haptic microscope (SHM),” *J. Artif. Organs*, vol. 14, no. 4, pp. 276–283, Dec. 2011.

[19] T. Krüger, K. Veseli, H. Lausberg, L. Vöhringer, W. Schneider, and C. Schlensak, “Regional and directional compliance of the healthy aorta: an ex vivo study in a porcine model,” *Interact. Cardiovasc. Thorac. Surg.*, vol. 23, no. 1, pp. 104–111, Jul. 2016.

[20] T. T. Tanaka and Y.-C. Fung, “Elastic and inelastic properties of the canine aorta and their variation along the aortic tree,” *J. Biomech.*, vol. 7, no. 4, pp. 357–370, Aug. 1974.

[21] D. Haskett, G. Johnson, A. Zhou, U. Utzinger, and J. Vande Geest, “Microstructural and biomechanical alterations of the human aorta as a function of age and location,” *Biomech. Model. Mechanobiol.*, vol. 9, no. 6, pp. 725–736, Dec. 2010.

[22] C. M. He and M. R. Roach, “The composition and mechanical properties of abdominal aortic aneurysms,” *J. Vasc. Surg.*, vol. 20, no. 1, pp. 6–13, Jul. 1994.

[23] M. L. Harkness, R. D. Harkness, and D. A. McDonald, “The collagen and elastin content of the arterial wall in the dog.,” *Proc. R. Soc. London. Ser. B, Biol. Sci.*, vol. 146, no. 925, pp. 541–51, Jun. 1957.

[24] V. Saey, N. Famaey, M. Smoljkic, E. Claeys, G. Van Loon, R. Ducatelle, M. Ploeg, C. Delesalle, A. Gröne, L. Duchateau, and K. Chiers, “Biomechanical and biochemical properties of the thoracic aorta in warmblood horses, Friesian horses, and Friesians with aortic rupture,” *BMC Vet. Res.*, vol. 11, no. 285, 2015.

[25] J. M. Davidson, K. E. Hill, M. L. Mason, and M. G. Giro$, “Longitudinal Gradients of Collagen Porcine Aorta* and Elastin Gene Expression in the,” *J. Biol. Chem.*, vol. 260, no. 3, pp. 1301–1908, 1985.

[26] J. Concannon, P. Dockery, A. Black, S. Sultan, N. Hynes, P. E. McHugh, K. M. Moerman, and J. P. McGarry, “Quantification of the regional bioarchitecture in the

human aorta," *J. Anat.*, p. joa.13076, Sep. 2019.

[27] R. H. Mohiaddin, S. R. Underwood, H. G. Bogren, D. N. Firmin, R. H. Klipstein, and D. B. Longmore, "Regional aortic compliance studied by magnetic resonance imaging: the effects of age, training, and coronary artery disease," *Br Hear. J*, vol. 62, pp. 90–6, 1989.

[28] T. Länne, B. Sonesson, D. Bergqvist, H. Bengtsson, and D. Gustafsson, "Diameter and compliance in the male human abdominal aorta: Influence of age and aortic aneurysm," *Eur. J. Vasc. Surg.*, vol. 6, no. 2, pp. 178–184, Mar. 1992.

[29] D. R. Nolan and J. P. McGarry, "On the Compressibility of Arterial Tissue," *Ann. Biomed. Eng.*, vol. 44, no. 4, pp. 993–1007, Apr. 2016.

[30] J. P. McGarry, J. Fu, M. T. Yang, C. S. Chen, R. M. McMeeking, A. G. Evans, and V. S. Deshpande, "Simulation of the contractile response of cells on an array of micro-posts," *Philos. Trans. R. Soc. A Math. Phys. Eng. Sci.*, vol. 367, no. 1902, pp. 3477–3497, Sep. 2009.

[31] W. M. Swanson and R. E. Clark, "Dimensions and Geometric Relationships of the Human Aortic Value as a Function of Pressure," *Circ. Res.*, vol. 35, no. 6, pp. 871–882, Dec. 1974.

[32] P. Kochova, Z. Tonar, V. M. Matejka, J. Sviglerova, M. Stengl, and J. Kuncova, "Morphology and mechanical properties of the subrenal aorta in normotensive and hypertensive rats.," *Biomed. Pap. Med. Fac. Univ. Palacky. Olomouc. Czech. Repub.*, vol. 152, no. 2, pp. 239–245, 2008.

[33] K. Khanafer, M. S. Schlicht, and R. Berguer, "How should we measure and report elasticity in aortic tissue?," *Eur. J. Vasc. Endovasc. Surg.*, vol. 45, no. 4, pp. 332–339, Apr. 2013.

[34] A. N. Azadani, S. Chitsaz, A. Mannion, A. Mookhoek, A. Wisneski, J. M. Guccione, M. D. Hope, L. Ge, and E. E. Tseng, "Biomechanical Properties of Human Ascending Thoracic Aortic Aneurysms," *Ann. Thorac. Surg.*, vol. 96, pp. 50–58, 2013.

[35] M. Gabriela Espinosa, M. Catalin Staiculescu, J. Kim, E. Marin, and J. E. Wagenseil, "Elastic Fibers and Large Artery Mechanics in Animal Models of Development and Disease.," *J. Biomech. Eng.*, vol. 140, no. 2, 2018.

[36] P. B. Dobrin, W. H. Baker, and W. C. Gley, "Elastolytic and Collagenolytic Studies of Arteries: Implications for the Mechanical Properties of Aneurysms," *Arch. Surg.*, vol. 119, no. 4, pp. 405–409, 1984.

[37] G. Faury, M. Pezet, R. H. Knutsen, W. A. Boyle, S. P. Heximer, S. E. McLean, R. K. Minkes, K. J. Blumer, A. Kovacs, D. P. Kelly, D. Y. Li, B. Starcher, and R. P. Mecham, "Developmental adaptation of the mouse cardiovascular system to elastin haploinsufficiency.," *J. Clin. Invest.*, vol. 112, no. 9, pp. 1419–28, Nov. 2003.

[38] C. Bellini, M. R. Bersi, A. W. Caulk, J. Ferruzzi, D. M. Milewicz, F. Ramirez, D. B. Rifkin, G. Tellides, H. Yanagisawa, and J. D. Humphrey, "Comparison of 10 murine models reveals a distinct biomechanical phenotype in thoracic aortic aneurysms," *J. R. Soc. Interface*, vol. 14, no. 130, May 2017.

[39] J. G. Barra, R. L. Armentano, J. Levenson, E. I. C. Fischer, R. H. Pichel, and A. Simon, "Assessment of smooth muscle contribution to descending thoracic aortic

elastic mechanics in conscious dogs," *Circ. Res.*, vol. 73, no. 6, pp. 1040–1050, 1993.

[40] R. J. Coulson, M. J. Cipolla, L. Vitullo, and N. C. Chesler, "Mechanical properties of rat middle cerebral arteries with and without myogenic tone.," *J. Biomech. Eng.*, vol. 126, no. 1, pp. 76–81, Feb. 2004.

[41] G. A. Holzapfel, T. C. Gasser, and R. W. Ogden, "A New Constitutive Framework for Arterial Wall Mechanics and a Comparative Study of Material Models," *J. Elast. Phys. Sci. solids*, vol. 61, no. 1–3, pp. 1–48, 2000.

[42] S. Zeinali-Davarani, Y. Wang, M.-J. Chow, R. € El Turcotte, and Y. Zhang, "Contribution of Collagen Fiber Undulation to Regional Biomechanical Properties Along Porcine Thoracic Aorta," *J. Biomech. Eng.*, vol. 137, 2015.

[43] J. D. Humphrey, "Possible mechanical roles of glycosaminoglycans in thoracic aortic dissection and associations with dysregulated transforming growth factor-β," *Journal of Vascular Research*, vol. 50, no. 1. pp. 1–10, Dec-2012.

[44] P. P. Weafer, W. Ronan, S. P. Jarvis, and J. P. McGarry, "Experimental and Computational Investigation of the Role of Stress Fiber Contractility in the Resistance of Osteoblasts to Compression," *Bull. Math. Biol.*, vol. 75, no. 8, pp. 1284–1303, Aug. 2013.

[45] E. McEvoy, V. S. Deshpande, and P. McGarry, "Transient active force generation and stress fibre remodelling in cells under cyclic loading," *Biomech. Model. Mechanobiol.*, vol. 18, no. 4, pp. 921–937, Aug. 2019.

[46] N. H. Reynolds and J. P. McGarry, "Single cell active force generation under dynamic loading - Part II: Active modelling insights," *Acta Biomater.*, vol. 27, pp. 251–263, Nov. 2015.

[47] N. H. Reynolds, W. Ronan, E. P. Dowling, P. Owens, R. M. McMeeking, and J. P. McGarry, "On the role of the actin cytoskeleton and nucleus in the biomechanical response of spread cells," *Biomaterials*, vol. 35, no. 13, pp. 4015–4025, Apr. 2014.

[48] E. P. Dowling, W. Ronan, and J. P. McGarry, "Computational investigation of in situ chondrocyte deformation and actin cytoskeleton remodelling under physiological loading," *Acta Biomater.*, vol. 9, no. 4, pp. 5943–5955, Apr. 2013.

[49] E. McEvoy, G. A. Holzapfel, and P. McGarry, "Compressibility and Anisotropy of the Ventricular Myocardium: Experimental Analysis and Microstructural Modeling," *J. Biomech. Eng.*, vol. 140, no. 8, Aug. 2018.

[50] J. Bols and J. Vierendeels, "Inverse modelling of image-based patient-specific blood vessels: zero-pressure geometry and in vivo stress incorporation," *ESAIM Math. Model. Numer. Anal.*, 2013.

[51] K. Krishnan, L. Ge, H. Haraldsson, M. D. Hope, D. A. Saloner, J. M. Guccione, and E. E. Tseng, "Ascending thoracic aortic aneurysm wall stress analysis using patient-specific finite element modeling of *in vivo* magnetic resonance imaging," *Interact. Cardiovasc. Thorac. Surg.*, vol. 21, no. 4, pp. 471–480, Oct. 2015.

[52] C. Martin, W. Sun, and J. Elefteriades, "Patient-specific finite element analysis of ascending aorta aneurysms," *Am. J. Physiol. Circ. Physiol.*, vol. 308, no. 10, pp. H1306–H1316, May 2015.

[53] G. Martufi, A. Forneris, S. Nobakht, K. D. Rinker, R. D. Moore, and E. S. Di Martino, "Case Study: Intra-Patient Heterogeneity of Aneurysmal Tissue Properties," *Front. Cardiovasc. Med.*, vol. 5, p. 82, Jul. 2018.

[54] S. Pasta, J.-S. Cho, O. Dur, K. Pekkan, and D. A. Vorp, "Computer modeling for the prediction of thoracic aortic stent graft collapse," *J. Vasc. Surg.*, vol. 57, no. 5, pp. 1353–1361, May 2013.

[55] P. Erhart, C. Grond-Ginsbach, M. Hakimi, F. Lasitschka, S. Dihlmann, D. Böckler, and A. Hyhlik-Dürr, "Finite element analysis of abdominal aortic aneurysms: predicted rupture risk correlates with aortic wall histology in individual patients.," *J. Endovasc. Ther.*, vol. 21, no. 4, pp. 556–64, Aug. 2014.

[56] A. Finotello, S. Morganti, and F. Auricchio, "Finite element analysis of TAVI: Impact of native aortic root computational modeling strategies on simulation outcomes," *Med. Eng. Phys.*, vol. 47, pp. 2–12, Sep. 2017.

[57] A. Dumenil, A. Kaladji, M. Castro, S. Esneault, A. Lucas, M. Rochette, C. Goksu, and P. Haigron, "Finite-element-based matching of pre-and intraoperative data for image-guided endovascular aneurysm repair," *IEEE Trans. Biomed. Eng.*, vol. 60, no. 5, pp. 1353–1362, 2013.

[58] R. R. F. Stevens, A. Grytsan, J. Biasetti, J. Roy, M. L. Liljeqvist, and T. Christian Gasser, "Biomechanical changes during abdominal aortic aneurysm growth," *PLoS One*, vol. 12, no. 11, Nov. 2017.

[59] B. E. Burkhardt, N. Byrne, M. N. Velasco Forte, F. Iannaccone, M. De Beule, G. J. Morgan, and T. Hussain, "Evaluation of a modified Cheatham-Platinum stent for the treatment of aortic coarctation by finite element modelling," *JRSM Cardiovasc. Dis.*, vol. 7, p. 204800401877395, Jan. 2018.

[60] L. Emerel, J. Thunes, T. Kickliter, M. Billaud, J. A. Phillippi, D. A. Vorp, S. Maiti, and T. G. Gleason, "Predissection-derived geometric and distensibility indices reveal increased peak longitudinal stress and stiffness in patients sustaining acute type A aortic dissection: Implications for predicting dissection," *J. Thorac. Cardiovasc. Surg.*, vol. 158, no. 2, pp. 355–363, Aug. 2019.

[61] A. J. Schriefl, T. Schmidt, D. Balzani, G. Sommer, and G. A. Holzapfel, "Selective enzymatic removal of elastin and collagen from human abdominal aortas: Uniaxial mechanical response and constitutive modeling," *Acta Biomater.*, vol. 17, pp. 125–136, 2015.

[62] M. Bloksgaard, T. M. Leurgans, B. Spronck, M. H. G. Heusinkveld, B. Thorsted, K. Rosenstand, I. Nissen, U. M. Hansen, J. R. Brewer, L. A. Bagatolli, L. M. Rasmussen, A. Irmukhamedov, K. D. Reesink, and J. G. R. De Mey, "Imaging and modeling of acute pressure-induced changes of collagen and elastin microarchitectures in pig and human resistance arteries," *Am. J. Physiol. Circ. Physiol.*, vol. 313, no. 1, pp. H164–H178, Jul. 2017.

[63] M.-J. Chow, R. Turcotte, C. P. Lin, and Y. Zhang, "Arterial Extracellular Matrix: A Mechanobiological Study of the Contributions and Interactions of Elastin and Collagen," *Biophys. J.*, vol. 106, pp. 2684–2692, 2014.

[64] J. M. Mattson and Y. Zhang, "Structural and Functional Differences Between Porcine Aorta and Vena Cava.," *J. Biomech. Eng.*, vol. 139, no. 7, p. 0710071, Jul. 2017.

[65] J. Zhang, X. Zhao, D. E. Vatner, T. McNulty, S. Bishop, Z. Sun, Y.-T. Shen, L. Chen, G. A. Meininger, and S. F. Vatner, "Extracellular Matrix Disarray as a Mechanism for Greater Abdominal Versus Thoracic Aortic Stiffness With Aging in Primates.," *Arterioscler. Thromb. Vasc. Biol.*, vol. 36, no. 4, pp. 700–6, Apr. 2016.

[66] J. Zhang, X. Zhao, D. E. Vatner, T. McNulty, S. Bishop, Z. Sun, Y.-T. Shen, L. Chen, G. A. Meininger, and S. F. Vatner, "Extracellular Matrix Disarray as a Mechanism for Greater Abdominal Versus Thoracic Aortic Stiffness With Aging in Primates.," *Arterioscler. Thromb. Vasc. Biol.*, vol. 36, no. 4, pp. 700–6, Apr. 2016.

[67] A. V. Kamenskiy, Y. A. Dzenis, S. A. J. Kazmi, M. A. Pemberton, I. I. Pipinos, N. Y. Phillips, K. Herber, T. Woodford, R. E. Bowen, C. S. Lomneth, and J. N. MacTaggart, "Biaxial mechanical properties of the human thoracic and abdominal aorta, common carotid, subclavian, renal and common iliac arteries," *Biomech. Model. Mechanobiol.*, vol. 13, no. 6, pp. 1341–1359, Oct. 2014.

[68] J. A. Peña, V. Corral, M. A. Martínez, and E. Peña, "Over length quantification of the multiaxial mechanical properties of the ascending, descending and abdominal aorta using Digital Image Correlation," *J. Mech. Behav. Biomed. Mater.*, vol. 77, pp. 434–445, Jan. 2018.

[69] J. Blacher, R. Asmar, S. Djane, G. M. London, and M. E. Safar, "Aortic pulse wave velocity as a marker of cardiovascular risk in hypertensive patients.," *Hypertens. (Dallas, Tex. 1979)*, vol. 33, no. 5, pp. 1111–7, May 1999.

[70] M. Vyas, J. Izzojr, Y. Lacourciere, J. Arnold, M. Dunlap, J. Amato, M. Pfeffer, and G. Mitchell, "Augmentation Index and Central Aortic Stiffness in Middle-Aged to Elderly Individuals," *Am. J. Hypertens.*, vol. 20, no. 6, pp. 642–647, Jun. 2007.

[71] A. Lalande, P. Khau Van Kien, P. M. Walker, L. Zhu, L. Legrand, M. Claustres, X. Jeunemaître, F. Brunotte, and J. E. Wolf, "Compliance and pulse wave velocity assessed by MRI detect early aortic impairment in young patients with mutation of the smooth muscle myosin heavy chain," *J. Magn. Reson. Imaging*, vol. 28, no. 5, pp. 1180–1187, Nov. 2008.

[72] C. V Ioannou, D. R. Morel, A. N. Katsamouris, S. Katranitsa, I. Startchik, A. Kalangos, N. Westerhof, and N. Stergiopulos, "Left ventricular hypertrophy induced by reduced aortic compliance.," *J. Vasc. Res.*, vol. 46, no. 5, pp. 417–25, 2009.

[73] A. Duprey, K. Khanafer, M. Schlicht, S. Avril, D. Williams, and R. Berguer, "In Vitro Characterisation of Physiological and Maximum Elastic Modulus of Ascending Thoracic Aortic Aneurysms Using Uniaxial Tensile Testing," *Eur. J. Vasc. Endovasc. Surg.*, vol. 39, no. 6, pp. 700–707, 2010.

[74] R. N. Isnard, B. M. Pannier, S. Laurent, G. M. London, B. Diebold, and M. E. Safar, "Pulsatile diameter and elastic modulus of the aortic arch in essential hypertension: A noninvasive study," *J. Am. Coll. Cardiol.*, vol. 13, no. 2, pp. 399–405, Feb. 1989.

[75] R. Behkam, K. E. Roberts, A. J. Bierhals, M. E. Jacobs, J. D. Edgar, R. C. Paniello, G. Woodson, J. P. Vande Geest, and J. M. Barkmeier-Kraemer, "Aortic arch compliance and idiopathic unilateral vocal fold paralysis," *J. Appl. Physiol.*, vol. 123, no. 2, pp. 303–309, Aug. 2017.

[76] M. Schäfer, L. P. Browne, G. J. Morgan, A. J. Barker, B. Fonseca, D. D. Ivy, and M. B. Mitchell, "Reduced proximal aortic compliance and elevated wall shear stress after

early repair of tetralogy of Fallot," *J. Thorac. Cardiovasc. Surg.*, vol. 156, no. 6, pp. 2239–2249, Dec. 2018.

[77] M. A. Lillie, M. A. Piscitelli, A. W. Vogl, J. M. Gosline, and R. E. Shadwick, "Cardiovascular design in fin whales: High-stiffness arteries protect against adverse pressure gradients at depth," *J. Exp. Biol.*, vol. 216, no. 14, pp. 2548–2563, Jul. 2013.

[78] R. Shadwick and J. M. Gosline, "MECHANICAL PROPERTIES OF THE OCTOPUS AORTA," 1985.

[79] J. Vychytil, F. Moravec, P. Kochová, J. Kuncová, and J. ˇ Svíglerová, "Modelling of the mechanical behaviour of porcine carotid artery undergoing inflation-deflation test," 2010.

[80] G. J. Langewouters, K. H. Wesseling, and W. J. Goedhard, "The static elastic properties of 45 human thoracic and 20 abdominal aortas in vitro and the parameters of a new model.," *J. Biomech.*, vol. 17, no. 6, pp. 425–35, 1984.

[81] J. J. Wang, S. H. Liu, T. Kao, W. C. Hu, and C. P. Liu, "Noninvasive determination of arterial pressure-dependent compliance in young subjects using an arterial tonometer," *Biomed. Eng. - Appl. Basis Commun.*, vol. 18, no. 3, pp. 111–118, Jun. 2006.

[82] F. J. H. Gijsen, J. J. Wentzel, A. Thury, B. Lamers, J. C. H. Schuurbiers, P. W. Serruys, and A. F. van der Steen, "A new imaging technique to study 3-D plaque and shear stress distribution in human coronary artery bifurcations in vivo," *J. Biomech.*, vol. 40, no. 11, pp. 2349–2357, 2007.

[83] F. J. H. Gijsen, J. C. H. Schuurbiers, A. G. van de Giessen, M. Schaap, A. F. W. van der Steen, and J. J. Wentzel, "3D reconstruction techniques of human coronary bifurcations for shear stress computations," *J. Biomech.*, vol. 47, no. 1, pp. 39–43, Jan. 2014.

[84] K. M. Moerman, "GIBBON: The Geometry and Image-Based Bioengineering add-On," *J. Open Source Softw.*, vol. 3, no. 22, p. 506, 2018.

[85] M. K. O'Connell, S. Murthy, S. Phan, C. Xu, J. Buchanan, R. Spilker, R. L. Dalman, C. K. Zarins, W. Denk, and C. A. Taylor, "The three-dimensional micro- and nanostructure of the aortic medial lamellar unit measured using 3D confocal and electron microscopy imaging," *Matrix Biol.*, vol. 27, no. 3, pp. 171–181, Apr. 2008.

[86] A. J. Schriefl, G. Zeindlinger, D. M. Pierce, P. Regitnig, and G. A. Holzapfel, "Determination of the layer-specific distributed collagen fibre orientations in human thoracic and abdominal aortas and common iliac arteries.," *J. R. Soc. Interface*, vol. 9, no. 71, pp. 1275–86, Jun. 2012.

[87] L. . Bostan, C. Noble, and N. Smulders, "Measurement of friction-induced changes in pig aorta fibre organization by non-invasive imaging as a model for detecting the tissue response to endovascular catheters," *Biotribology*, 2016.

[88] X. Yu, Y. Wang, and Y. Zhang, "Transmural variation in elastin fiber orientation distribution in the arterial wall," *J. Mech. Behav. Biomed. Mater.*, vol. 77, pp. 745–753, Jan. 2018.

[89] L. Horny, J. Kronek, H. Chlup, R. Zitny, J. Vesely, and M. Hulam, "Orientations of collagen fibers in aortic histological section," *Bull. Appl. Mech.*, vol. 6, no. 22, pp. 25–29, 2010.

[90] É. Ó. Máirtín, G. Parry, G. E. Beltz, and J. P. McGarry, "Potential-based and non-potential-based cohesive zone formulations under mixed-mode separation and over-closure-Part II: Finite element applications," *J. Mech. Phys. Solids*, vol. 63, no. 1, pp. 363–385, Feb. 2014.

[91] J. P. McGarry and P. E. McHugh, "Modelling of in vitro chondrocyte detachment," *J. Mech. Phys. Solids*, vol. 56, no. 4, pp. 1554–1565, Apr. 2008.

[92] E. M. Feerick and J. P. McGarry, "Cortical bone failure mechanisms during screw pullout," *J. Biomech.*, vol. 45, no. 9, pp. 1666–1672, Jun. 2012.